Heliyon 9 (2023) e13634

Contents lists available at ScienceDirect

Heliyon

journal homepage: www.cell.com/heliyon

Research article

The impact of horizontal eye movements versus intraocular pressure on optic nerve head biomechanics: A tridimensional finite element analysis study

Diana Marcela Muñoz Sarmiento [a,b,c,*], Óscar Libardo Rodríguez Montaño [a], Juan David Alarcón Castiblancoa [a], Carlos Julio Cortés Rodríguez [a]

[a] Grupo de Investigación en Biomecánica, Universidad Nacional de Colombia, Colombia
[b] Sociedad de Oftalmología Eduardo Arenas Archila, Colombia
[c] Laboratorio de Anatomía y Fisiología, Grupo de Ciencias Básicas y Laboratorios, Universidad Manuela Beltrán, Colombia

ARTICLE INFO

Keywords:
Finite element
Glaucoma
Optic nerve
Eye movements
Ocular movements
Biomechanics
Physiopathology
Papilledema
Subarachnoid space
Intraocular pressure

ABSTRACT

It has been proposed that eye movements could be related to glaucoma development. This research aimed to compare the impact of intraocular pressure (IOP) versus horizontal duction on optic nerve head (ONH) strains. Thus, a tridimensional finite element model of the eye including the three tunics of the eye, all of the meninges, and the subarachnoid space (SAS) was developed using a series of medical tests and anatomical data. The ONH was divided into 22 subregions, and the model was subjected to 21 different eye pressures, as well as 24 different degrees of adduction and abduction ranging from 0.5° to 12°. Mean deformations were documented along anatomical axes and in principal directions. Additionally, the impact of tissue stiffness was assessed. The results show no statistically significant differences between the lamina cribrosa (LC) strains due to eye rotation and IOP variation. However, when assessing LC regions some experienced a reduction in principal strains following a 12° duction, while after the IOP reached 12 mmHg, all LC subzones showed an increase in strains. From an anatomical perspective, the effect on the ONH following 12° duction was opposite to that observed after a rise in IOP. Moreover, high strain dispersion inside the ONH subregions was obtained with lateral eye movements, which was not observed with increased IOP and variation. Finally, SAS and orbital fat stiffness strongly influenced ONH strains during eye movements, while SAS stiffness was also influential under ocular hypertension. Even if horizontal eye movements cause large ONH deformations, their biomechanical effect would be markedly distinct from that induced by IOP. It could be predicted that, at least in physiological conditions, their potential to cause axonal injury would not be so relevant. Thus, a causative role in glaucoma does not appear likely. By contrast, an important role of SAS would be expectable.

1. Introduction

Currently, glaucoma is the leading cause of irreversible blindness worldwide [1]. It constitutes a group of optic neuropathies characterized by progressive degeneration of retinal ganglion cells (RGC). These cells are neurons that have their cell bodies inside the

* Corresponding author. Grupo de Investigación en Biomecánica, Universidad Nacional de Colombia, Colombia.
E-mail address: dmmunozs@unal.edu.co (D.M. Muñoz Sarmiento).

https://doi.org/10.1016/j.heliyon.2023.e13634
Received 25 August 2022; Received in revised form 31 January 2023; Accepted 6 February 2023
Available online 11 February 2023

retina and their axons in the optic nerve. The classic physiopathology theory of glaucoma poses that an increase in intraocular pressure (IOP) would lead to compression of the axons at the lamina cribrosa (LC) with consequent ischemia and axoplasmic flow blockage, and hence the death of RGC [2]. However, although high IOP is recognized as the most important risk factor for glaucoma [3], this is not the only mechanical load experienced by the optic nerve, as it is also influenced by cerebrospinal fluid pressure [4,5], IOP fluctuations [6], vascular pulsatility [7], and eye movements [8–20], among other factors.

Regarding the latter, Wang et al. [8], through finite element (FE) analysis, compared the ONH strains (engineering definition of deformation) induced by 13° lateral eye movements to those resulting from an increase in IOP from 15 to 50 mmHg, finding that mean and peak strains due to ocular movements were significantly higher than those due to increased IOP. Likewise, Shin et al. [9] studied ONH stresses and strains during 6° adduction vs multiple levels of IOP in an FE model, concluding that adduction produces far greater mechanical stress and strain than does IOP elevation. A recent FE study performed by Jafari et al. [10], in which a 6° ocular rotation was generated, has also confirmed these findings. Thus, as a result, it has been hypothesized that eye movements could also contribute to the development of glaucomatous optic neuropathy [8,9,11,12].

Despite this, while experimentally *in vivo* important levels of deformation in the ONH have been observed following horizontal eye rotation [13–17], no significant differences have been documented with strains associated with an increase in IOP [18–20]. In this respect, Wang et al. [19] studied 16 eyes from 8 healthy subjects, in which LC strains were induced by horizontal duction and an acute IOP elevation; average LC strains were 6.41% with a mean IOP elevation of 21.13 mmHg, 5.83% for 20° adduction, and 3.93% for 20° abduction. Chuangsuwanich et al. [20] assessed ONH strains in 74 healthy, primary open-angle glaucoma, normal tension glaucoma, and highly myopic subjects, finding that in all groups, adduction produced ONH strains of the same order of magnitude (3.4%) as those induced by an IOP of 40 mmHg (3.8%), whereas abduction generated significantly lower strains (2.8%). Finally, Hoang et al. [18] reported that in myopic eyes ONH strains are equally influenced by IOP elevation and adduction.

Besides that, to the best of our knowledge, eye movements have not been recognized as a glaucoma risk factor in clinical settings [21,22], and even when eye movement alterations have been reported in glaucoma patients [23–25], this could primarily be the result of visual pathway and cortex damage observed in this disease [26–30], rather than a direct mechanical injury. In this sense, glaucoma could not be mechanically caused by ocular movements.

On the other hand, eye anatomy has typically been reconstructed variably in FE studies. As a result, different eye regions and tissues have been included and excluded in posterior ocular models [8–12,31–37]. Biologically the eye is comprised of three tunics, namely: fibrous (cornea and sclera), vascular (iris, ciliary body, and choroid), and nervous (retina), and it is located within the orbit and surrounded by fat [38]. In addition, the optic nerve emerges from its posterior pole and is enveloped by a series of layers called the meninges: pia mater, arachnoid, and dura mater; in between the pia mater and arachnoid, there is a space called the subarachnoid space (SAS) [39].

Nevertheless, some ocular models have not included the choroid [8–10,12,31,32,34,36,37], and some others neither the nervous tunic [9,10,12,33]. Besides that, the retina has usually been regarded as an extension of the prelaminar tissue [40] and adipose tissue has not been commonly incorporated. Regarding the optic nerve, typically, the complete meningeal layers have not been included, and in some cases, only the pia mater has been added [31,33,36]. In this respect, in a prior FE study we found that ONH strains decreased considerably when meninges were progressively integrated [35], which suggests that anatomical variability and oversimplification may result in inaccuracy [41].

Furthermore, the optic nerve's SAS has been commonly modeled as empty, with the cerebrospinal fluid pressure (CSFP) applied inside it [8,9,11,12,31–34,37]. However, the SAS is not an empty space; rather, it is a complex structure that includes very dense layers of trabeculae, collagen-based structures that act as supportive pillars between the arachnoid and the pia mater [39,42–44], and allow the flow of cerebrospinal fluid among its spaces. This creates a complex solid–fluid interaction and helps damp and protect the delicate nervous tissue from mechanical damage [44,45], whereby it can modify the stresses and strains experienced by the ONH nervous tissue during eye rotations and ocular hypertension. Consequently, including the SAS could be of special relevance.

Previously, the present authors reported that under conditions of ocular hypertension, the Young's modulus of the SAS strongly influences ONH and peripapillary region strains [35]; nevertheless, regarding eye movements, the role of the SAS has not yet been

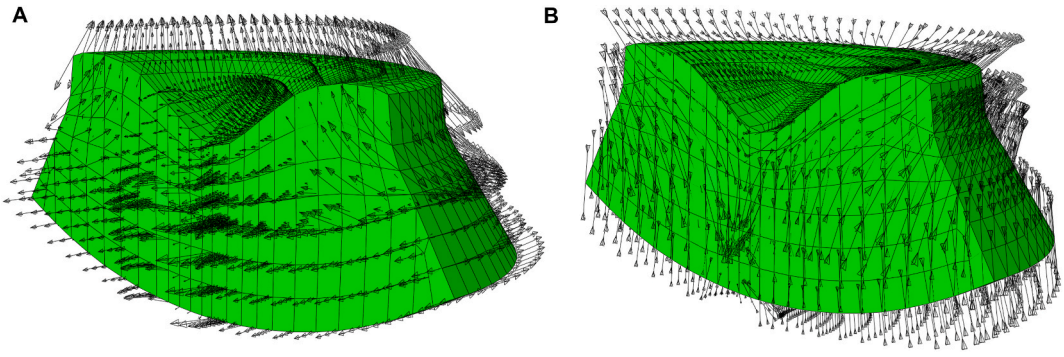

Fig. 1. The vectors that characterize (A) the maximum principal directions, and (B) the minimum principal directions inside the lamina cribrosa and prelaminar tissue after an IOP increase of 12 mmHg can be appreciated. Note the diverse directions in which they are oriented.

previously explored.

Moreover, the use of mechanical properties from different anatomical regions and species has also been common. Since tissue behavior varies among species and the different anatomical locations from which it is extracted [46,47], a major error factor could be introduced.

Lastly, computational studies have primarily focused on the analysis of strains and stresses in the maximum and minimum principal directions [8–12,31,32,34,36,37], which represent the largest stretching and shortening experienced by the tissues [8], respectively. By contrast, clinical and experimental research has studied ONH deformations and displacements mainly in the anteroposterior and

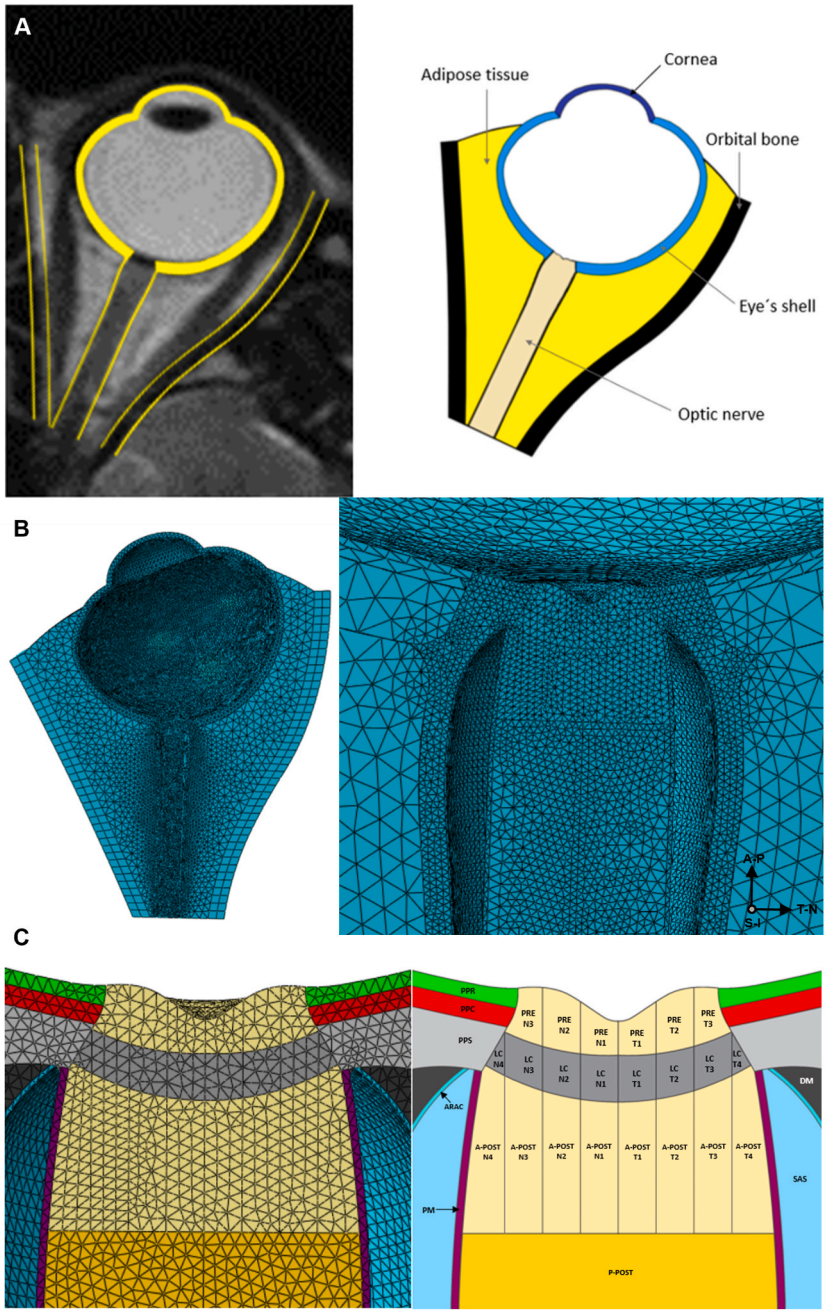

Fig. 2. A. Finite element model boundary superimposed on the MR scan in the primary gaze position and the reconstructed geometry. B. Finite element mesh of the ocular model, orbit and optic nerve. C. Reconstructed anatomy and mesh of the optic nerve head and peripapillary region. Note the subregions in which the optic nerve head was segmented: N (nasal region), T (temporal region), PPR (peripapillary retina), PPC (peripapillary choroid), PPS (peripapillary sclera), PRE (prelaminar tissue), LC (lamina cribosa), A-POST (anterior-postlaminar tissue), P-POST (posterior-postlaminar tissue), PM (piamater), SAS (subarachnoid space), ARAC (arachnoids), DM (duramater).

radial directions [48–52]. Even though strains in the maximum and minimum principal directions represent extreme deformations, the direction of the vector that characterizes them varies at each calculated point inside the tissues (Fig. 1A–B), whereby their pathophysiological effect could vary. Thus, determining the stresses and strains in anatomical axes is also necessary to accomplish a complete physiopathological analysis.

The purpose of this study was to establish the acute effects of IOP variations versus (vs) abduction and adduction on ONH strains along the principal directions and anatomical axes: temporal–nasal (T-N), anterior–posterior (A-P) and superior–inferior (S–I), particularly in the LC. As part of this research, the impact of including the SAS in optic nerve deformations during ocular rotation is also explored. To achieve this, a tridimensional (3D) finite model of the orbit and eye was built including the three tunics of the eye, peripapillary region, optic nerve neural tissue, and all of the meninges.

2. Methods

2.1. 3D geometrical reconstruction

Representing eye anatomy accurately is challenging due to the complexity of this organ. To overcome this, a 30-year-old woman without any medical or ophthalmological antecedent underwent a complete ophthalmological examination by a glaucoma specialist and a battery of medical tests in the primary gaze position in both eyes, namely orbital magnetic resonance (MR); orbital computed axial tomography (CT); pachymetry; ONH, macular, and anterior segment high-resolution optical coherence tomography (OCT); and optical coherence tomography angiography, among others, all of which were conducted in accordance with ethical guidelines, previous approval from the Ethics Committee of the Faculty of Medicine of the National University of Colombia, and prior informed consent. The above, on one hand, ensured the patient's normal condition, and on the other, enabled better anatomical reconstruction.

In this way, outlines of the cornea and sclera of the right eye were manually delineated from the MR in the transverse plane, and then their width was adjusted based on data from the patient's test and earlier research [53]. Accordingly, based on OCT data, the central corneal thickness was 535 μm, and the lateral was adjusted using pachymetry. The scleral thickness varied from 390 μm at the peripapillary flange to 940 μm at the posterior pole and 420 μm at the equator [53]. At the limbus, scleral width was fixed from the lateral corneal thickness and gradually decreased to the equator as informed by Vurgese et al. [53].

Subsequently, the peripapillary retina and choroid were included, with thicknesses of 116 μm (OCT data) and 155 μm [54,55], respectively, and were then extended along the scleral shell. Since MR examination of the corneoscleral shape revealed approximate symmetry between the right and left sides of the right eye, the left side of the right eye was revolutionized to obtain an initial 3D eye shell model (Fig. 2A).

Furthermore, the optic nerve anatomy included the prelaminar neural tissue, LC, postlaminar neural tissue, SAS, and all of the meninges (pia mater, dura mater, and arachnoid). The prelaminar tissue contained ONH excavation, and the cup/disk ratio was adjusted to 0.46 (the patient-reported OCT value). The LC had a central thickness of 0.37 mm [56] and a lateral thickness of 0.30 mm [31]. The pia mater and arachnoid had a constant width of 0.06 and 0.03 mm [35], respectively, while the dura mater thickness was 0.4 mm and became thicker close to the sclera [8]. The SAS was thicker in the anterior part and then became progressively thinner [57]. Later, the optic nerve was embedded into the ocular globe shell, its length was adjusted using MR measurements, and CT and MR scans were used to build orbital fat and bone, thus generating a complete orbital 3D reconstruction (Fig. 2B). Note that to lessen the computational time, only half the model was built.

As a final step, to obtain a more detailed analysis of the ONH, postlaminar tissue was segmented into anterior (1 mm from the scleral canal) and posterior regions [32,35]; subsequently, the LC was subdivided into eight concentric zones from its center (four nasal and four temporal), which were then extended to the prelaminar and postlaminar regions, thus obtaining six subregions in the prelaminar tissue and eight in the postlaminar tissue, giving a total of 22 ONH subregions (Fig. 2C).

2.2. Mechanical properties

To achieve accurate predictions with the FE method, selection of the appropriate tissue properties is required. For the above, in this study special emphasis has been placed on selecting human data and physiological testing conditions, when available. In addition, data from locations other than the eyeball and orbit have been also avoided. Although this could result in the use of simpler material models in some anatomical regions, it could also lead to greater biological accuracy.

Thus, the cornea, peripapillary sclera, posterior sclera, dura mater, and choroid were modeled as hyperelastic, homogeneous, isotropic, and incompressible, considering in this way their nonlinear behavior [8,10,46,58]. The retina was also modeled following this approach since Chen et al. [46] reported that it exhibits slightly nonlinear behavior. Hence, experimental data describing the stress–strain curve for each tissue were digitized and fitted to hyperelastic models.

Additionally, because the ocular globe and optic nerve are made up of tiny structures that are difficult to access, even today, there is a lack of information on the mechanical properties of human optic nerve tissues [8,32]. For this reason, the pia mater, arachnoid, prelaminar tissue, LC, and postlaminar tissue were assumed to be isotropic, homogeneous, and linearly elastic [31,35]; as in earlier research, these tissues were considered almost incompressible.

Thus, a Young's modulus of 0.3 MPa was assigned to the pia mater [31]. Similarly, due to the absence of measurements of arachnoid mechanical properties in the optic nerve and other anatomical zones, a Young's modulus of 0.3 MPa was assumed (same as pia mater) [35]. This was because both leptomeninges have similar histological composition [59].

Regarding human prelaminar tissue, postlaminar tissue, and LC, the available information is particularly sparse. Thus, although

ONH modeling is complex (especially the LC), these tissues were modeled from the estimations of Sigal et al. [31], which have been validated by recent *in vivo* research [40], as a result, biological precision would be ensured. This was also done because different studies have shown a good linear fit for LC and neural tissue at strains less than 13% [60–62], which was obtained in our preliminary simulations (a maximum strain of 9.6%, 13.2%, and 13.3%, for LC, prelaminar, and postlaminar tissue, respectively).

Similarly, the orbital bone was also modeled with a linear elastic behavior because previous studies showed a good linear fit at low deformations [63,64], and because our preliminary analysis confirmed small strains during ocular rotations and IOP fluctuations. Finally, for simplicity, a linear elastic approach was also used to model orbital fat [65]. All the above allowed us to obtain an initial foundation to investigate the eye's mechanical behavior (Table 1).

2.3. Boundary conditions

All tissues were tied together at their interface, except between the sclera and orbital fat, where a frictionless contact was employed (simulating the Tenon's capsule space) [8]. A contact with a frictional coefficient of 0.5 was used between adipose tissue and bone [8]; in this way, the fatty tissue slid over the bone as previously informed by Wang et al. [8]. Furthermore, the optic nerve was fixed at the orbital canal level, simulating the fibrous bands in this anatomical region [57]. Symmetry boundary conditions were imposed, and the external surface of the orbital bone was fixed [8].

2.4. Loading conditions

Different loading scenarios were considered to estimate ONH strains. In the first scenario, IOP was applied to the inner limiting membrane and then gradually increased in increments of 2.5 mmHg, from 2.5 to 50 mmHg, for a total of 20 IOP values, corresponding to normal (10–20 mmHg), hypotension (less than 10 mmHg), and hypertension spectrums (greater than 20 mmHg). No ocular rotation was imposed in this case, and a CSFP of 10 mmHg was applied (a normal value in the supine position).

In a second scenario, a fixed IOP of 15 mmHg and a CSFP of 10 mmHg were imposed, and a rotation was applied directly to the external surface of the sclera, simulating in this way the effect of the extraocular muscles, and achieving a turn in the transverse plane with zero rotation in the other anatomical planes. Abduction and adduction were increased progressively in 0.5° increments, from 0.5° to 12°, for a total of 48 rotations (24 in abduction and 24 in adduction), and strains for the different ONH anatomical regions and subregions were obtained. Finally, in a third scenario, an IOP increase of 12 mmHg (from 15 to 27 mmHg) with 0° of rotation and a CSFP of 10 mmHg was generated.

2.5. Numerical details

The model was created, meshed, and solved in Abaqus®, where the previously described properties, interactions, loads, and boundaries were established. Heterogeneous tetrahedral and hexahedral meshing elements were employed, using tetrahedra for all the anatomical regions except orbital bone (Fig. 2B). Furthermore, to provide numerical accuracy in the zones of interest without

Table 1
Mechanical properties assigned to the tissues.

Tissue	Specie	Anatomical region	Constitutive model	Properties (MPa)	Reference
Cornea	Human	Ocular globe	Reduced polynomial 2	$C_{10} = 0.1$, $C_{20} = 0.9$, $D_1 = 0$, $D_2 = 0$	58
Prelaminar tissue	Estimated data	Optic nerve	Linear elastic	Young's Modulus (E) = 0.03, Poisson's ratio (ν) = 0.49	31
Postlaminar tissue	Estimated data	Optic nerve	Linear elastic	Young's Modulus (E) = 0.03, Poisson's ratio (ν) = 0.49	31
Lamina cribosa	Human	Optic nerve	Linear elastic	Young's Modulus (E) = 0.3, Poisson's ratio (ν) = 0.49	31
Retina	Human	Ocular globe	Reduced polynomial 5	$C_{10} = 1.9$, $C_{20} = 0.4$, $C_{30} = -77.9$, $C_{40} = 6346.0$, $C_{50} = 9559.7$, $D_1 = 0$, $D_2 = 0$, $D_3 = 0$, $D_4 = 0$, $D_5 = 0$	46
Choroid	Human	Ocular globe	Reduced polynomial 5	$C_{10} = 9.3$, $C_{20} = 7.9$, $C_{30} = 0.8$, $C_{40} = -4.6$, $C_{50} = 7.7$, $D_1 = 0$, $D_2 = 0$, $D_3 = 0$, $D_4 = 0$, $D_5 = 0$	46
Posterior sclera	Human	Ocular globe	Reduced polynomial 6	$C_{10} = 3.2E\text{-}02$, $C_{20} = 1.4$, $C_{30} = -6.8$, $C_{40} = 21.1$, $C_{50} = -30.5$, $C_{60} = 16.4$, $D_1 = 0$, $D_2 = 0$, $D_3 = 0$, $D_4 = 0$, $D_5 = 0$, $D_6 = 0$	46
Peripapillary sclera	Human	Ocular globe	Reduced polynomial 5	$C_{10} = 0.4$, $C_{20} = 8.4$, $C_{30} = 2.2$, $C_{40} = -3.5$, $C_{50} = 1.5$, $D_1 = 0$, $D_2 = 0$, $D_3 = 0$, $D_4 = 0$, $D_5 = 0$	10
Pia mater	Estimated data	Optic nerve	Linear elastic	Young's Modulus (E) = 3, Poisson's ratio (ν) = 0.49	31
Arachnoid	Estimate data	Optic nerve	Linear elastic	Young's Modulus (E) = 3, Poisson's ratio (ν) = 0.49	35
Dura mater	Porcine	Optic nerve	Ogden 3	$\mu_1 = -91.0$, $\mu_2 = 61.8$, $\mu_3 = 29.6$, $\alpha_1 = 2.0$, $\alpha_2 = 4.0$, $\alpha_3 = -2.0$, $D_1 = 0$, $D_2 = 0$, $D_3 = 0$	8
Peri orbitary fat tissue	Human	Orbital cavity	Linear elastic	Young's Modulus (E) = 0.0083, Poisson's ratio (ν) = 0.49	65
Orbital bone	Human	Orbital cavity	Linear elastic	Young's Modulus (E) = 15200, Poisson's ratio (ν) = 0.3	63,64

generating an excessive computational cost, 10-node tetrahedral elements were used in the ONH and peripapillary regions, while in other regions 4-node tetrahedral elements were employed [66].

The element size in the ONH, peripapillary region, and adjacent meninges was approximately 100 μm [9]. In the other anatomical zones, it varied between 100 and 1000 μm, ensuring precision in the relevant areas, while minimizing the number of elements as previously described by Shin et al. [9], which was numerically validated through a convergence test. As a result, the model included approximately 809.729 elements and required approximately 6 h to complete each simulation (CPU time).

2.6. Postprocessing analysis

Numerical artifacts such as irregularly shaped elements can generate extreme values affecting the results [32]. Therefore, in this study, a 10% bounded mean was calculated for the strains in each region and subregion of the ONH, at each IOP, and each degree of horizontal duction. Peak strains were not included as part of this study, because the primary goal was to assess global ONH damage, which would negatively affect functional reserve, decreasing physiological activity and leading to disease development.

Subsequently, using the bounded mean values, a linear regression was performed to obtain the slope that describes the strain change per 1 mmHg (Δ Strain (%)/Δ mmHg), as well as the strain change per 1° of abduction and adduction (Δ Strain (%)/Δ °). Some of the results are presented in the form of mean ± standard deviation, range: minimum–maximum value.

In addition, changes in ONH strains after an IOP increase of 12 mmHg from baseline (IOP of 15 mmHg with 0° of rotation) were compared to those following a 12° horizontal duction from baseline. Note that for the results extracted from each simulation, the coordinate reference system was adjusted in such a way that it was always aligned with the LC and ONH center [15].

2.7. Model comparison

To ensure adequate predictions, a series of the patient's orbital MR scans at different degrees of horizontal duction were acquired, and the outline of the FE model for each case was superimposed and qualitatively compared, as reported by Wang et al. [8]. Furthermore, LC and prelaminar mean displacement results were compared quantitatively with data from the clinical study by Fazio et al. [67], in which a very acute elevation (1 min) of IOP in normal patients was carried out.

2.8. SAS inclusion

To assess the impact of SAS inclusion, as an initial approach, the empty space with the CSFP was replaced by the SAS. The SAS in cranial studies has been typically modeled as soft solid, fluid, or porous medium [44]. In this regard, Saboori et al. [44] conducted a comprehensive study to determine the appropriate modeling of SAS material, and their findings revealed that the three above-mentioned models are equally adequate and reliable. They also determined that the optimum elastic modulus of the SAS is approximately 1150 Pa and the Poisson ratio is 0.48 [68]. Therefore, for simplicity, the SAS was modeled as a linearly elastic soft solid with the values recommended by these authors. Strains from rotating the eye from 0.5° to 12°, varying the IOP from 2.5 mmHg to 50 mmHg, and comparing a 12 mmHg IOP increase vs 12° of adduction and abduction were obtained as previously described.

2.9. Variation of eye tissue stiffness

Because the stiffness of eye tissues varies among individuals, a study of the influence of the eye tissue stiffness under 12° abduction, 12° adduction, and 50 mmHg IOP was conducted. For simplicity, in this assay, all tissues were assumed to be isotropic, linear-elastic, and homogeneous, so stiffness could be described by a single quantity: Young's modulus [69]. So, Young's modulus was increased and decreased by 20% and 40% from the baseline value (Table 2) and then a linear regression was performed, obtaining the strain change per MPa for each tissue (Δ Strain (%)/Δ MPa). The IOP and CSFP were also varied, and the slopes obtained (Δ Strain (%)/Δ MPa) were

Table 2
Linear mechanical properties assigned to the tissues.

Tissue	Specie	Anatomical region	Constitutive model	Properties	Reference
Cornea	Human	Ocular globe	Linear elastic	$E = 1.3$ MPa, $\nu = 0.42$	58
Prelaminar tissue	Estimated data	Optic nerve	Linear elastic	$E = 0.03$ MPa, $\nu = 0.49$	31
Postlaminar tissue	Estimated data	Optic nerve	Linear elastic	$E = 0.03$ MPa, $\nu = 0.49$	31
Lamina cribosa	Estimated data	Optic nerve	Linear elastic	$E = 0.3$ MPa, $\nu = 0.49$	31
Retina	Human	Ocular globe	Linear elastic	$E = 0.015$ MPa, $\nu = 0.49$	46
Choroid	Human	Ocular globe	Linear elastic	$E = 0.375$ MPa, $\nu = 0.49$	46
Posterior sclera	Human	Ocular globe	Linear elastic	$E = 4.4$ MPa, $\nu = 0.49$	46
Peripapillary sclera	Monkey	Ocular globe	Linear elastic	$E = 4.1$ MPa, $\nu = 0.49$	69
Pia mater	Estimated data	Optic nerve	Linear elastic	$E = 3$ MPa, $\nu = 0.49$	31
Arachnoid	Estimated data	Optic nerve	Linear elastic	$E = 3$ MPa, $\nu = 0.49$	35
SAS	Estimated data	Cranial cavity	Linear elastic	$E = 0.00115$ MPa, $\nu = 0.48$	44,68
Dura mater	Porcine	Optic nerve	Linear elastic	$E = 5.2$ MPa, $\nu = 0.49$	8
Peri orbitary fat tissue	Human	Orbital cavity	Linear elastic	$E = 0.0083$ MPa, $\nu = 0.49$	65
Orbital bone	Human	Orbital cavity	Linear elastic	$E = 15200$ MPa, $\nu = 0.3$	63,64

compared; 320 simulations were run in total.

3. Results

3.1. Comparison with orbital magnetic resonance

A good match between the FE model and MR in the primary and rotated positions was observed (Fig. 3A–C). Moreover, the absolute and relative error of mean prelaminar and laminar displacement compared to clinical data were, respectively, 2.40 μm and 68.68% for the model excluding SAS, and 2.40 μm and 68.52% for the model with SAS (Table 3).

3.2. IOP increase of 12 mmHg vs 12° eye rotation

3.2.1. ONH strains: prelaminar, laminar, and postlaminar regions

Elevation of the IOP by 12 mmHg and rotation of the eye by 12° had different biomechanical effects on the ONH. In this way, from the perspective of the principal direction, elevating the IOP resulted in an increase in strains throughout the ONH, with the highest values in the LC, and comparatively lower values in the prelaminar and postlaminar tissue.

In contrast, after 12° abduction and adduction, the prelaminar and postlaminar regions experienced a significant increase in strains, with far lower values than in the LC. Besides that, far higher strains were obtained in prelaminar and postlaminar regions when compared to IOP elevation. This means that extreme values of compression and stretching would be increased so much more in the LC after IOP elevation than following horizontal ocular movements. Despite these differences between ocular duction and IOP elevation, they were not statistically significant ($p = 0.51$, Friedman test).

From the anatomical perspective, after a 12 mmHg IOP elevation, the ONH experienced compression in the A–P direction, with the greatest values of increase in the LC; and stretching along the S–I. In terms of the T–N axis, LC and postlaminar tissues stretched, while prelaminar tissue compressed. After horizontal duction, the ONH primarily suffered elongation in the A–P direction and compression in the S–I axis, with variable results for the T–N direction ($p = 0.64$, Friedman test). As a result, the biomechanical effect of elevating the IOP vs rotating the eye on the ONH was not equivalent (Fig. 4).

3.2.2. ONH strains by subzones

When considering the subregions, it became evident that horizontal eye movements impacted the ONH markedly differently than increased IOP. For instance, there was a reduction of strains in the minimum and maximum principal directions resulting from 12°

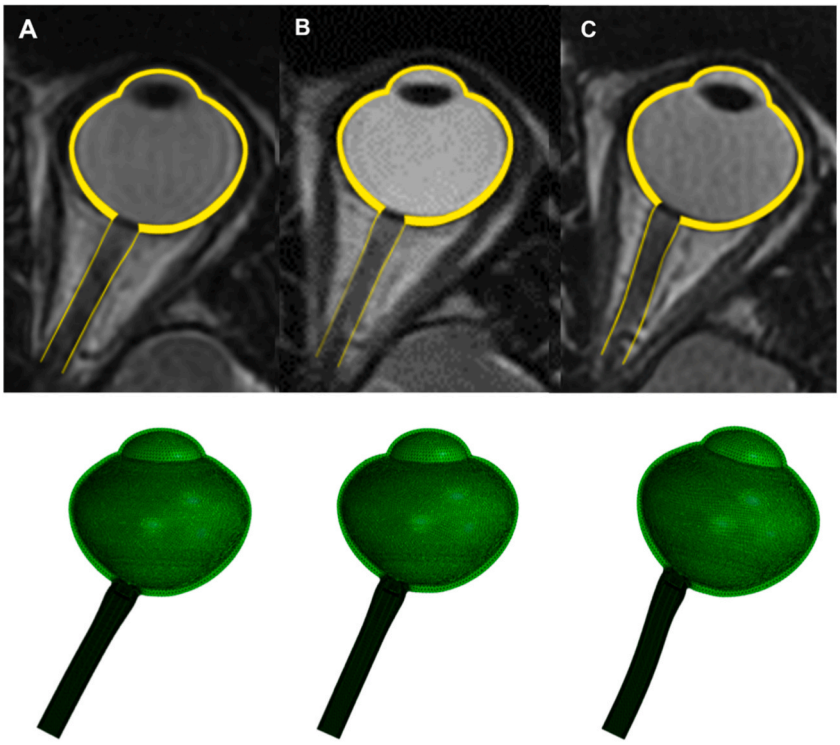

Fig. 3. Finite element model boundary superimposed on the MR scan after a 3° adduction **(A)**, in the primary gaze position **(B)**, and after a 12° abduction **(C)**.

Table 3
Model results compared with data from clinical study.

	Specie	Time (minutes)	Reported absolute Δ μm/Δ mmHg	Δ μm/Δ mmHg Model with SAS	Δ μm/Δ mmHg Model without SAS	Absolute error Model with SAS	Relative error Model with SAS	Absolute error Model without SAS	Relative error Model without SAS
PRE	Human	1	3.40	1.23	1.24	2.17	63.85%	2.16	63.44%
PRE	Human	1	3.27	1.23	1.24	2.04	62.41%	2.03	61.98%
LC	Human	1	3.34	0.94	0.91	2.40	71.82%	2.43	72.63%
LC	Human	1	3.92	0.94	0.91	2.98	75.99%	3.01	76.68%

horizontal ocular movements in the central laminar regions, while strains increased in the lateral ones. After a 12 mmHg IOP elevation, conversely, strains raised throughout all of the LC subregions in a more homogeneous distribution pattern (Supplementary Material 1).

Thus, in general terms, a 12 mmHg IOP elevation led to a strain pattern of effect inside the ONH, much more uniformly than 12° horizontal ocular duction (less data dispersion induced by increased IOP in all examined directions). This was true for each of the ONH regions (prelaminar tissue, LC, and postlaminar tissue), was statically significant (Table 4), and confirmed for all of the different levels

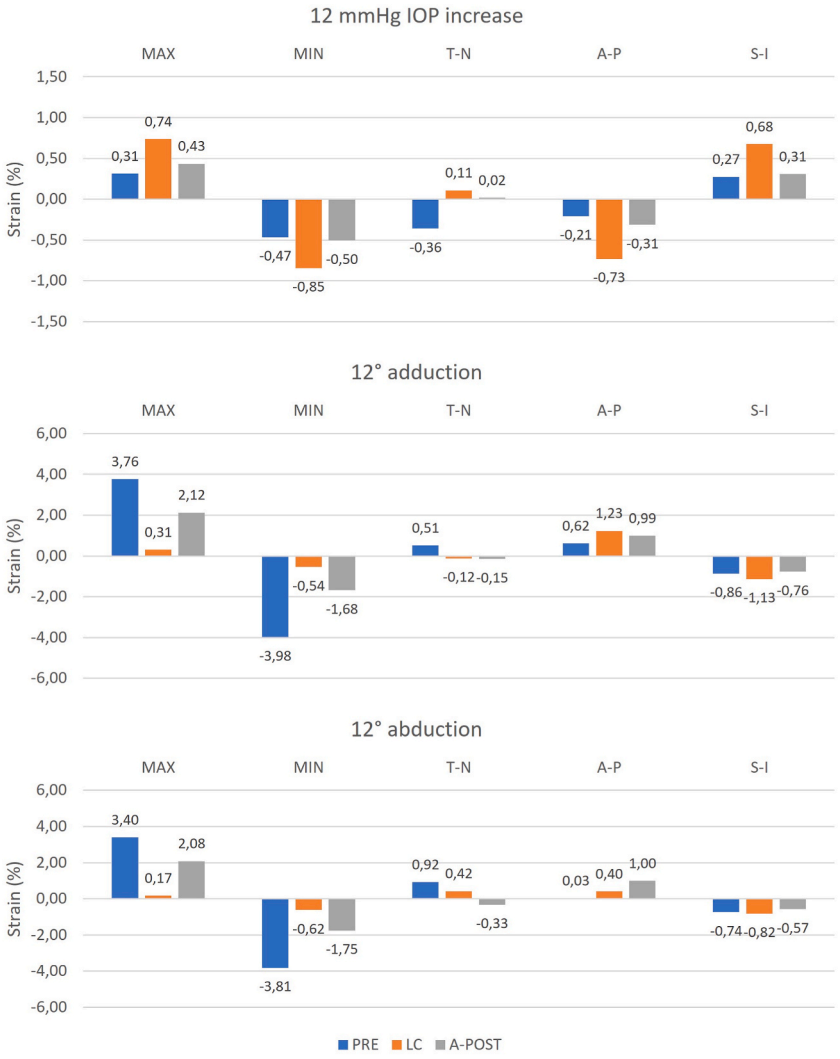

Fig. 4. Computed strains in the maximum principal direction (MAX), minimum principal direction (MIN), and anatomical axes (T-N, A-P, and S–I) for each biological region following an IOP increase of 12 mmHg, a 12° adduction, and a 12° adduction. A positive value in the maximum principal direction indicates an increase in strains, while a negative value indicates a decrease. A negative value in the minimum principal direction indicates an increase in strains, while a positive value indicates a decrease. A positive value in the anatomical directions indicates an elongation, while a negative value indicates a shortening.

of IOP and ocular rotation generated in the present study.

Furthermore, abduction and adduction influenced the ONH differently. For example, A–P laminar stretching was increased in adduction towards the nasal subregions, and in abduction towards the temporal subregions; the prelaminar and postlaminar regions, in general terms, were accompanied by a temporal elongation and nasal compression along the A–P axis following adduction, which was reversed in abduction. In contrast, after IOP elevation, the central nasal and temporal regions experienced the greatest values of strain, with a tendency to decline toward lateral ones for all the evaluated directions. Complete results for subzones can be viewed in Supplementary Material 1.

3.3. Influence of ocular rotations and IOP variations on LC strains

Fig. 5 shows each of the results obtained for the LC, and Table 5 presents each of the computed slopes for the LC. A good linear correlation was obtained in all directions ($R^2 = 0.97 \pm 0.03$, range: 0.92–1.00; $p = 0.00 \pm 0.00$, range: 0.00–0.00). This shows that, in the maximum and minimum principal directions, the LC experienced a decrease in strain with the beginning of ocular rotation, followed by an increase in strain as the degrees of rotation augmented. As regards the anatomical axes, important changes in deformations were also observed with the start of eye rotation. There were no statistically significant differences in the calculated LC slopes among IOP fluctuation, adduction, and abduction ($p = 0.57$, Friedman test).

3.4. Influence of ocular rotations and IOP variations on prelaminar and postlaminar strains

3.4.1. Model with SAS

For the model including the SAS, after 12° ocular rotation and a 12 mmHg increase in IOP, the SAS was the anatomical structure experiencing the highest strain levels within the optic nerve, in both principal and anatomical directions, with far greater strains comparatively with other anatomical regions. This was particularly true following lateral eye movements, during which the levels of strains were at a maximum and would reflect its damping role in the course of ocular movements and IOP fluctuations (Fig. 6).

There were no statistically significant differences between ONH strain values and those of the model without the SAS, following 12° ocular adduction ($p = 0.98$, Mann–Whitney U test), 12° abduction ($p = 0.93$, Mann–Whitney U test), or 12 mmHg IOP elevation ($p = 0.97$, Mann–Whitney U test), although the same patterns were not observed (Supplementary Material 2).

Moreover, there was a trend toward ONH compression along the A–P axis and stretching along the S–I axis induced by an increase in IOP, unlike horizontal duction, which induced mainly elongation in the A–P direction and compression along the S–I axis; the above is in agreement with the findings for the model excluding the SAS. Additionally, as previously obtained, the differences in the ONH strains between ocular duction and IOP elevation were not statistically significant ($p = 0.86$, Friedman test).

Upon examination of the ONH subzones, the differences in comparison with the model without the SAS were not significant after 12° ocular adduction ($p = 0.71$, Mann–Whitney U test), 12° abduction ($p = 0.67$, Mann–Whitney U test), and 12 mmHg IOP elevation ($p = 0.99$, Mann–Whitney U test), although the same patterns were not obtained.

As in the model without the SAS, there was an important increase of laminar strains in all subzones after a 12 mmHg rise in IOP in the principal directions, and a reduction in central laminar strains in maximum and minimum principal directions following lateral ocular movements. In addition, as previously documented, ONH strain dispersion among subzones was far greater after 12° horizontal duction than after a 12 mmHg increase in IOP ($p = 0.00$, Friedman test).

Finally, regarding LC slopes, no statistically significant differences were found in adduction ($p = 0.94$, Mann–Whitney U test),

Table 4
Computed standard deviations of strains among the subzones of the prelaminar tissue, lamina cribosa, and anterior-postlaminar tissue in the maximum principal direction (MAX), minimum principal direction (MIN), and anatomical axes (T-N, A-P, and S–I). Higher values of dispersion for the 12° horizontal duction than the 12 mmHg IOP increase can be observed.

Prelaminar tissue					
	MAX	MIN	T-N	A-P	S–I
12 mmHg IOP increase	0.08	0.05	0.07	0.19	0.11
12° adduction	0.42	1.01	1.18	1.95	1.03
12°abduction	0.36	0.68	1.14	1.93	1.00
Lamina cribosa					
	MAX	MIN	T-N	A-P	S–I
12 mmHg IOP increase	0.08	0.19	0.12	0.24	0.12
12° adduction	0.76	0.77	0.73	0.73	0.24
12°abduction	0.66	0.63	0.73	0.74	0.20
Anterior-postlaminar tissue					
	MAX	MIN	T-N	A-P	S–I
12 mmHg IOP increase	0.15	0.13	0.09	0.30	0.20
12° adduction	1.14	0.67	0.62	1.31	0.64
12°abduction	1.21	0.66	0.66	1.37	0.66
p (Friedman test)	0.00				

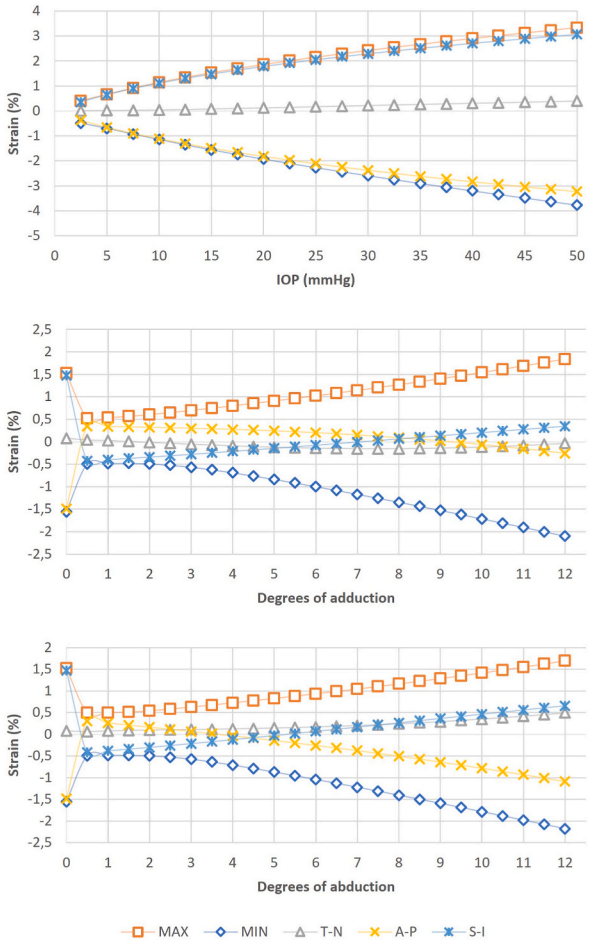

Fig. 5. Strains obtained for lamina cribosa when varying the IOP and rotating the eyeball horizontally in the maximum principal direction (MAX), minimum principal direction (MIN), and anatomical axes (T-N, A-P, and S–I).

Table 5
Calculated slopes in the maximum principal direction (MAX), minimum principal direction (MIN), and anatomical directions (T-N, A-P, and S–I) for the lamina cribosa. The structures with only MAX, MIN, T-N, A-P, and S–I indicate a single behavior; structures including the subindex 2 indicate a mixed behavior depending on the considered range.

	MAX	MIN	T-N	$T\text{-}N_2$	A-P	S–I
Δ strain (%)/Δ mmHg	0.06	−0.07	0.01	–	−0.06	0.05
Δ strain (%)/Δ °(adduction)	0.12	−0.15	−0.03	0.03	−0.05	0.07
Δ strain (%)/Δ °(abduction)	0.11	−0.16	0.03	–	−0.12	0.09
p (Friedman test)	0.57					

abduction ($p = 0.92$, Mann–Whitney *U* test), or IOP variation ($p = 1.0$, Mann–Whitney *U* test) between the models with and without the SAS. Complete results for the model including the SAS can be found in Supplementary Material 2.

3.4.2. Variation of eye tissue stiffness

A good linear correlation was obtained in all directions ($R^2 = 0.97 \pm 0.06$, range: 0.35–1.00; $p = 0.01 \pm 0.04$, range: 0.41–0.00). Variations in IOP, CSFP, orbital fat tissue, and SAS stiffness had the strongest influence on strains during ocular rotations, while under ocular hypertension IOP and CSFP had the greatest impact. SAS stiffness was also influential during hypertensive ocular conditions (Supplementary Material 3).

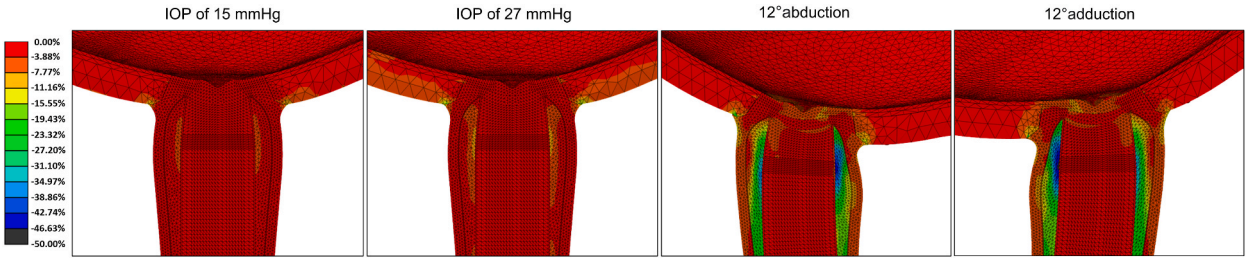

Fig. 6. Strains in the minimum principal direction for various loading scenarios. A negative value indicates a shortening experienced by the tissues. Note the high deformation values in the SAS.

4. Discussion

The FE method is a well-established tool for biomechanical research. It provides detailed information on strains and stresses that is too difficult to obtain experimentally [70]. As a result, different authors have investigated the mechanical impact of horizontal ocular movements on ONH biomechanics using FE analysis, finding far greater strains and stresses than those caused by increased IOP [8,9,11], thereby supporting the theory that repetitive strain during eye movements may injure the ONH.

In this research, however, while large strains were found after horizontal duction, even exceeding several times those caused by IOP (particularly in prelaminar and postlaminar regions), no statistically significant differences due to IOP elevation and ocular rotation could be demonstrated, principally for the LC. Thus, the LC experienced larger deformations on average after a 12 mmHg IOP increase than after 12° duction, which is consistent with the report of Wang et al. [19]. For their part, prelaminar and postlaminar tissues deformed significantly more under 12° ocular rotation, with far higher values than under IOP elevation. In this way, IOP primarily affects the LC, while abduction and adduction affect the prelaminar and postlaminar regions. Furthermore, there were also significant differences when taking into account anatomical directions as well as ONH strain distributions across subzones.

This discrepancy with previous FE studies could be attributed to the preference for human data over that from other species in this research, as well as the avoidance of data from anatomical locations other than the eye and orbit. Similarly, in this study, we attempted to reconstruct the ocular anatomy as completely as possible, particularly in the posterior region of the eye and optic nerve. Despite the CPU time being longer than reported by previously published models (1.7 h with 4-noded tetrahedral 363,384 elements and 1.9 h when using 10-noded tetrahedral 371,992 elements) [66,71], this could result in a more realistic representation of the eye's behavior [41], as well as assessment of the impact of multiple tissues that interact *in vivo*.

In addition, a high degree of ONH segmentation was carried out and special emphasis was placed on anatomical directions, which helped to highlight the marked discrepancies between the impact of ocular duction and IOP elevation on ONH strains. Thus, when exploring the biomechanical effect of IOP vs horizontal duction from an anatomical perspective, the opposite effect was observed, especially for A–P and S–I axes. IOP elevation mostly produced an ONH compression in the A–P direction with stretching along the S–I axis; horizontal ocular duction principally produced ONH stretching in the A–P direction with compression along the S–I axis.

Regarding the latter, Wang et al. [19] reported a temporal pulling and nasal compression of the ONH in the transverse plane (A–P direction) following adduction, and compression of the prelaminar tissues following acute IOP elevation. Lee et al. [14] performed, in 52 healthy subjects, a 3D analysis of the ONH changes induced by lateral eye movements in the nasal and temporal regions, finding that overall, ONH was elevated in abduction, and in adduction, there was an elevation of the nasal side and depression of the temporal side. Suh et al. [15] studied the effect of a graded range of horizontal duction in 50 eyes of 25 normal subjects, finding that the optic nerve cup shifted anteriorly in abduction and showed little change in adduction. Demer et al. [16], employing MR imaging, reported that the optic nerve becomes more redundant and sinusoidal during abduction. For their part, Chuangsuwanich et al. [20] reported a prelaminar posterior displacement under IOP elevation. The results presented here are consistent with most of the above-reported experimental findings.

Because the ONH blood supply is primarily supplied by centripetal branches [57], the capillary network would preferentially run in the transverse plane. Since the A–P axis is orthogonal to this plane, compression in this direction would be expected to result in maximum shear stresses on the capillary walls and thus maximum blood flow blockage [72]. As a result, compression along the A–P axis could be likely to cause a greater ischemic effect than along the other anatomical axes. Hence, it could be hypothesized that an increase in IOP would have a much greater ischemic effect than lateral eye movements.

Additionally, ONH deformations induced by IOP are expected to have a more homogeneous distribution than those caused by horizontal ocular duction. In this respect, Beotra et al. [73] found no significant variations across LC sectors in healthy subjects in a quantitative *in vivo* analysis that assessed regional differences in IOP-induced LC strain. Thus, in physiopathological terms, this would imply that IOP elevation affects a greater number of axons simultaneously than lateral eye movements.

Furthermore, horizontal duction could cause a reduction in maximum and minimum principal strains in some LC regions, thus protecting the delicate axons passing through it during eye movements. This, added to the fact that ocular movements are characterized by a short duration [74,75], would lead to the suggestion that at least under physiological conditions, their potential to cause axonal insult would be far lower than that caused by IOP increase and oscillations, and therefore their role for the development of glaucoma could be not so relevant as previously proposed. Nevertheless, this could not hold true if the properties of the ocular tissues

were altered, leading to a different biomechanical behavior; unfortunately, at present, tissue stiffness data from glaucoma patients are still scarce in the literature, and further clarification by future research will be required.

By contrast, an important pathological role for horizontal ocular movements could be predicted in diseases accompanied by an incremented A–P elongation as well as an incremented S–I compression, such as intracranial hypertension [35]. This in fact has been previously reported: Sibony et al. [17] examined through spectral-domain OCT the effects of horizontal eye movements on the peripapillary basement membrane layer in 45 patients with acute intracranial hypertension and papilledema, 15 with anterior ischemic optic neuropathy, and 20 normal subjects, reporting that the changes in papilledema patients were much greater than the small changes seen in the other groups.

On the other hand, to the best of our knowledge, the SAS has received little attention in the field of computational ophthalmology. Since it would constitute the primary damping anatomical structure in the optic nerve [44,76], it could also play a crucial role in ONH biomechanics. In this regard, we previously hypothesized that the SAS could have a strong role in glaucoma [35]; interestingly, there is growing clinical evidence demonstrating optic nerve SAS morphological alterations in glaucoma patients (particularly normal tension glaucoma).

Thus, Cennamo et al. [77] reported that patients with primary open-angle glaucoma present a significantly smaller SAS in their optic nerve (3.54 mm) than do normal controls (3.87 mm). Liu et al. [78] measured the area of the optic nerve SAS in glaucoma patients and controls, finding smaller values in normal tension glaucoma (5.15 mm^2) compared to normal controls (6.40 mm^2). For their part, Wang et al. [79] found that the SAS is narrower in normal tension glaucoma patients than in high-pressure or control groups. In addition, a narrower SAS has also been reported in myopia [80], a well-known glaucoma risk factor.

A reduced SAS could imply less damping capacity, making the ONH more vulnerable to mechanical loads and potentially increasing strains during IOP fluctuations and ocular movements. In this regard, Chuangsuwanich et al. [20] reported that normal tension glaucoma and highly myopic subjects exhibited larger strains *in vivo* during adduction than did controls. Hoang et al. [18] documented abnormally high strains in pathologically myopic eyes (6.6%) when compared to highly myopic eyes (3.4%) and slightly myopic eyes (2.6%) under an IOP elevation; they also found a similar tendency regarding eye movements. This will need to be clarified by further research.

Furthermore, the results of this study indicate that SAS stiffness, which represents SAS trabecular stiffness, would significantly modify ONH strains during IOP increase and eye movements. In this regard, the possibility of the SAS being linked to glaucoma pathogenesis seems highly probable. This will be addressed in future studies by the current authors.

Moreover, adipose orbital tissue stiffness would also have a significant influence on ONH strains in the course of eye movements because the rotation of the eye is partly explained by the sliding of Tenon's capsule and partly by the deformation of the orbital fat [81]. In this way, orbital fat would determine rotational stiffness [81], but also would modify strains in the ONH.

Finally, while no statistically significant differences were demonstrated between the model with and without the SAS, the deformation patterns for these two models were not exactly the same, which could lead to erroneous pathophysiological interpretations. Consequently, the development of a multiphysical model that allows for the integration of both the CSFP and the SAS damping effect would be of crucial importance to accurately simulate this complex organ. Meanwhile, to ensure correct predictions, any results from FE ocular models should be carefully checked through a comparison with available clinical and experimental research.

In summary, it could be predicted that horizontal eye movements would cause large strains in prelaminar and postlaminar regions, with lower strains comparatively in the LC, and even reduction in some LC subzones. Additionally, their anatomical effect would be the inverse of that induced by an increase in IOP, the IOP generating a greater effect on the LC, a homogeneous strain dispersion pattern inside the ONH, and compression along the A–P axis, with a likely sustained secondary ischemic effect, not expected during lateral eye movements. Consequently, this work does not support the idea that eye movements are a cause of optic nerve mechanical injury, and thus a cause of glaucoma; the SAS, on the other hand, could be thought to play an important mechanical role.

We would like to emphasize the importance of including anatomical axes as part of FE studies, since this allows for a more extensive physiopathological analysis, as well as a more complete comparison with prior published literature. As far as we know, this is the first FE study to pay special attention to anatomical directions and also to include the SAS.

5. Conclusion

Even if horizontal eye movements cause significant ONH deformation, their biomechanical effect would be markedly different from that of IOP. Thus, at least in physiological conditions, horizontal movements would not be expected to play an important role in glaucoma development. In contrast, the importance of the SAS could be hypothesized.

6. Limitations

This work has several limitations that merit further additional discussion. First, tissues were considered homogeneous and isotropic materials. Some tissues were assumed to be linearly elastic and others hyperelastic; nevertheless, biological tissues are neither homogeneous nor isotropic, and they display viscoelastic behavior. Particularly, the valuable anisotropic model of Girard et al. [82] could not be included as part of this research since at present it is not currently available in Abaqus®. Despite this, while the materials included do not reflect the exact mechanical behavior of tissues, they do represent an initial approximation.

Second, although a series of medical tests were carried out to achieve a more anatomical accurate model, some structures remain inaccessible to medical images; in consequence, generic data derived from human histological studies and anatomical descriptions had to be used for eye model reconstruction.

Third, although a 3D model was built, it does not reflect the exact anatomy and all the complexity of the human eye. In addition, even when a more complete anatomical model was achieved, some important anatomical structures, such as the vascular bed, Tenon's capsule, extraocular muscles, and LC microstructure, among others, are still missing in the model presented here. As regards the latter, some recent studies [36,83] have shown that at a microscale level, LC first principal strain can even exceed 20% in some regions. As a result, the impact of including a more detailed LC model in the results presented here is unknown.

Fourth, the ocular and orbit anatomy were reconstructed from a single eye, and the geometric model is not entirely patient-specific. Because eye anatomy differs among individuals, this could have a considerable influence on the ONH strains obtained in this study. Additionally, the morphology of glaucoma eyes could differ significantly.

Fifth, arachnoid stiffness was assumed to be equal to that of the pia mater. Even when both constitute leptomeninges [59,84], the arachnoid properties of the optic nerve could not be the same, and consequently, further clarification is necessary.

Sixth, in this work, only lateral eye movements were considered; a study of the effect of other types of duction on ONH biomechanics would also be of special value.

Seventh, SAS data properties were extracted from the cranial region, and similarly, dura mater properties did not come from humans, which introduces an additional bias. Additionally, the SAS damping function and CSFP were modeled separately; the outcome of integrating these two effects, and their impact on the results here described, is unknown.

Finally, the ONH strain values reported here are estimates based on FE analysis, not direct *in vivo* measurements. Since most of these measurements are not yet completely feasible, recent FE studies have compared model outlines with the shape of the eye in MR to ensure accurate predictions [8,10]. In this work, to guarantee predictability, a comparison with different studies in the literature has also been done (and is presented throughout the text), finding a high coincidence with prior *in vivo* human experimental and clinical research. Thus, interestingly, some of our FE predictions had already been previously documented by *in vivo* investigations. Furthermore, a comparison with mean ONH displacements reported in humans after a 1-min IOP increase was performed, obtaining a good quantitative match. However, in the future, further validation will be required.

Ethical statement

The authors declare that this work has followed all the ethical principles.

Author contribution statement

Diana Marcela Muñoz Sarmiento: Conceived and designed the experiments; Performed the experiments; Analyzed and interpreted the data; Wrote the paper. Óscar Libardo Rodríguez Montaño: Conceived and designed the experiments; Performed the experiments; Analyzed and interpreted the data. Juan David Alarcón Castiblanco: Conceived and designed the experiments; Performed the experiments. Carlos Julio Cortés Rodríguez: Contributed reagents, materials, analysis tools or data.

Funding statement

This research did not receive any specific grant from funding agencies in the public, commercial, or not-for-profit sectors.

Data availability statement

Data will be made available on request.

Declaration of competinginterest

The authors declare no competing interests.

Acknowledgments

The authors express all their gratitude to Doctor Eduardo Arenas, Professor of the Ophthalmology Department, for his invaluable support.

Appendix A. Supplementary data

Supplementary data to this article can be found online at https://doi.org/10.1016/j.heliyon.2023.e13634.

References

[1] Y.C. Tham, X. Li, T.Y. Wong, H.A. Quigley, T. Aung, C.Y. Cheng, Global prevalence of glaucoma and projections of glaucoma burden through 2040: a systematic review and meta-analysis, Ophthalmology 121 (2014) 2081–2090, https://doi.org/10.1016/j.ophtha.2014.05.013.

[2] R.N. Weinreb, T. Aung, F.A. Medeiros, The Pathophysiology and Treatment of Glaucoma A Review, 2014, https://doi.org/10.1001/jama.2014.3192.
[3] M.L. Salvetat, M. Zeppieri, C. Tosoni, P. Brusini, Continuing Medical Education: Baseline Factors Predicting the Risk of Conversion from Ocular Hypertension to Primary Open-Angle Glaucoma during a 10-year Follow-Up, 2016, https://doi.org/10.1038/eye.2016.86.
[4] J.B. Jonas, Role of cerebrospinal fluid pressure in the pathogenesis of glaucoma, Acta Ophthalmol. 89 (2011) 505–514, https://doi.org/10.1111/j.1755-3768.2010.01915.x.
[5] M. Greenwood, J. Berdahl, Cerebrospinal fluid pressure and glaucoma, J. Ophthalmic Vis. Res. 8 (2013) 180–186, https://doi.org/10.1007/s40135-016-0110-3.
[6] J. Caprioli, R. Varma, Intraocular pressure: modulation as treatment for glaucoma, Am. J. Ophthalmol. 152 (2011) 340–344.e2, https://doi.org/10.1016/J.AJO.2011.05.029.
[7] J.P.E. Stürmer, C. Kniestedt, [Role of ocular pulse amplitude in glaucoma], Klin Monbl Augenheilkd 232 (2015) 162–168, https://doi.org/10.1055/s-0034-1396232.
[8] X. Wang, H. Rumpe, W.E.H. Lim, M. Baskaran, S.A. Perera, M.E. Nongpiur, et al., Finite element analysis predicts large optic nerve head strains during horizontal eye movements, Invest. Ophthalmol. Vis. Sci. 57 (2016) 2452–2462, https://doi.org/10.1167/iovs.15-18986.
[9] A. Shin, L. Yoo, J. Park, J.L. Demer, Finite element biomechanics of optic nerve sheath traction in adduction, J. Biomech. Eng. 139 (2017), https://doi.org/10.1115/1.4037562.
[10] S. Jafari, Y. Lu, J. Park, J.L. Demer, Finite element model of ocular adduction by active extraocular muscle contraction, Invest. Ophthalmol. Vis. Sci. 62 (2021), https://doi.org/10.1167/IOVS.62.1.1.
[11] X. Wang, L.K. Fisher, D. Milea, J.B. Jonas, M.J.A. Girard, Predictions of optic nerve traction forces and peripapillary tissue stresses following horizontal eye movements, Invest. Ophthalmol. Vis. Sci. 58 (2017) 2044, https://doi.org/10.1167/IOVS.16-21319. –53.
[12] J. Park, A. Shin, J.L. Demer, Finite element modeling of effects of tissue property variation on human optic nerve tethering during adduction, Sci. Rep. 12 (2022), https://doi.org/10.1038/s41598-022-22899-2.
[13] M.Y. Chang, A. Shin, J. Park, A. Nagiel, R.A. Lalane, S.D. Schwartz, et al., Deformation of optic nerve head and peripapillary tissues by horizontal duction, Am. J. Ophthalmol. 174 (2017) 85–94, https://doi.org/10.1016/J.AJO.2016.10.001.
[14] W. June Lee, Y. Jeong Kim, J. Hong Kim, S. Hwang, S. Hak Shin, H. Woong LimID, Changes in the Optic Nerve Head Induced by Horizontal Eye Movements, 2018, https://doi.org/10.1371/journal.pone.0204069.
[15] S.Y. Suh, A. Le, A. Shin, J. Park, J.L. Demer, Progressive deformation of the optic nerve head and peripapillary structures by graded horizontal duction, Invest. Ophthalmol. Vis. Sci. 58 (2017) 5015–5021, https://doi.org/10.1167/IOVS.17-22596.
[16] J.L. Demer, Optic nerve sheath as a novel mechanical load on the globe in ocular duction, Invest. Ophthalmol. Vis. Sci. 57 (2016) 1826–1838, https://doi.org/10.1167/IOVS.15-18718.
[17] P.A. Sibony, Gaze evoked deformations of the peripapillary retina in papilledema and ischemic optic neuropathy, Invest. Ophthalmol. Vis. Sci. 57 (2016) 4979–4987, https://doi.org/10.1167/IOVS.16-19931.
[18] Q v Hoang, T. Chuangsuwanich, D.J.G. Yu, T.A. Tun, C.W. Wong, X. Wang, et al., Differing optic nerve head strains comparing low, high and pathologic myopia eyes, Invest. Ophthalmol. Vis. Sci. 61 (2020) 2679, 2679.
[19] X. Wang, M.R. Beotra, T.A. Tun, M. Baskaran, S. Perera, T. Aung, et al., In vivo 3-dimensional strain mapping confirms large optic nerve head deformations following horizontal eye movements, Invest. Ophthalmol. Vis. Sci. 57 (2016) 5825–5833, https://doi.org/10.1167/IOVS.16-20560.
[20] T. Chuangsuwanich, X. Wang, T.A. Tun, S.K. Devalla, D. Milea, Q v Hoang, et al., Adduction induces abnormally large optic nerve head strains in normal tension glaucoma subjects, Invest. Ophthalmol. Vis. Sci. 61 (2020) 1005, 1005.
[21] C.W. McMonnies, Glaucoma history and risk factors, J. Opt. 10 (2017) 71–78, https://doi.org/10.1016/J.OPTOM.2016.02.003.
[22] A. Worley, K. Grimmer-Somers, Risk factors for glaucoma: what do they really mean? Aust. J. Prim. Health 17 (2011) 233–239, https://doi.org/10.1071/PY10042.
[23] M.A. McDonald, C.H. Stevenson, H.M. Kersten, H v Danesh-Meyer, Eye movement abnormalities in glaucoma patients: a review, Eye Brain 14 (2022) 83–114, https://doi.org/10.2147/EB.S361946.
[24] S.S.Y. Lee, A.A. Black, J.M. Wood, Effect of glaucoma on eye movement patterns and laboratory-based hazard detection ability, PLoS One 12 (2017), https://doi.org/10.1371/journal.pone.0178876.
[25] S.S.Y. Lee, A.A. Black, J.M. Wood, Eye movements of drivers with glaucoma on a visual recognition slide test, Optom. Vis. Sci. 96 (2019) 484–491, https://doi.org/10.1097/OPX.0000000000001395.
[26] G. Michelson, S. Wärntges, T. Engelhorn, A. El-Rafei, J. Hornegger, A. Dörfler, [Integrity/demyelination of the optic radiation, morphology of the papilla, and contrast sensitivity in glaucoma patients], Klin Monbl Augenheilkd 229 (2012) 143–148, https://doi.org/10.1055/S-0031-1299262.
[27] A. El-Rafei, T. Engelhorn, S. Wärntges, A. Dörfler, J. Hornegger, G. Michelson, Glaucoma classification based on visual pathway analysis using diffusion tensor imaging, Magn. Reson. Imaging 31 (2013) 1081–1091, https://doi.org/10.1016/j.mri.2013.01.001.
[28] G. Michelson, T. Engelhorn, S. Wärntges, A. el Rafei, J. Hornegger, A. Doerfler, DTI parameters of axonal integrity and demyelination of the optic radiation correlate with glaucoma indices, Graefe's Arch. Clin. Exp. Ophthalmol. 251 (2013) 243–253, https://doi.org/10.1007/s00417-011-1887-2.
[29] R.W. Chan, J.W. Bang, V. Trivedi, M.C. Murphy, P. Liu, G. Wollstein, et al., Relationships between cerebrovascular reactivity, visual-evoked functional activity, and resting-state functional connectivity in the visual cortex and basal forebrain in glaucoma, Annu Int Conf IEEE Eng Med Biol Soc 2021 (2021) 4037–4040, https://doi.org/10.1109/EMBC46164.2021.9630904.
[30] R.O. Duncan, P.A. Sample, R.N. Weinreb, C. Bowd, L.M. Zangwill, Retinotopic organization of primary visual cortex in glaucoma: comparing fMRI measurements of cortical function with visual field loss, Prog. Retin. Eye Res. 26 (2007) 38–56, https://doi.org/10.1016/j.preteyeres.2006.10.001.
[31] I.A. Sigal, J.G. Flanagan, I. Tertinegg, C.R. Ethier, Finite element modeling of optic nerve head biomechanics, Invest. Ophthalmol. Vis. Sci. 45 (2004) 4378–4387, https://doi.org/10.1167/IOVS.04-0133.
[32] A.J. Feola, J.G. Myers, J. Raykin, L. Mulugeta, E.S. Nelson, B.C. Samuels, et al., Finite element modeling of factors influencing optic nerve head deformation due to intracranial pressure, Invest. Ophthalmol. Vis. Sci. 57 (2016) 1901–1911, https://doi.org/10.1167/IOVS.15-17573.
[33] A. Ayyalasomayajula, R.I. Park, B.R. Simon, J.P. vande Geest, A porohyperelastic finite element model of the eye: the influence of stiffness and permeability on intraocular pressure and optic nerve head biomechanics, Comput. Methods Biomech. Biomed. Eng. 19 (2016) 591–602, https://doi.org/10.1080/10255842.2015.1052417.
[34] Y. Mao, D. Yang, J. Li, J. Liu, R. Hou, Z. Zhang, et al., Finite element analysis of trans-lamina cribrosa pressure difference on optic nerve head biomechanics: the Beijing Intracranial and Intraocular Pressure Study, Sci. China Life Sci. 63 (2020) 1887, https://doi.org/10.1007/S11427-018-1585-8. –94.
[35] D.M. Muñoz-Sarmiento, Ó.L. Rodríguez-Montaño, J.D. Alarcón-Castiblanco, M.A. Gamboa-Márquez, J.P. Corredor-Gómez, C.J. Cortés-Rodríguez, A finite element study of posterior eye biomechanics: the influence of intraocular and cerebrospinal pressure on the optic nerve head, peripapillary region, subarachnoid space and meninges, Inform. Med. Unlocked 15 (2019), 100185, https://doi.org/10.1016/J.IMU.2019.100185.
[36] A. Karimi, S.M. Rahmati, R.G. Grytz, C.A. Girkin, J.C. Downs, Modeling the biomechanics of the lamina cribrosa microstructure in the human eye, Acta Biomater. 134 (2021) 357–378, https://doi.org/10.1016/J.ACTBIO.2021.07.010.
[37] Y. Hua, J. Tong, D. Ghate, S. Kedar, L. Gu, Intracranial pressure influences the behavior of the optic nerve head, J. Biomech. Eng. 139 (2017), https://doi.org/10.1115/1.4035406.
[38] B.D. Kels, A. Grzybowski, J.M. Grant-Kels, Human ocular anatomy, Clin. Dermatol. 33 (2015) 140–146, https://doi.org/10.1016/J.CLINDERMATOL.2014.10.006.
[39] J. Hao, C. Kohler, H. van den Dorpel, H.P.N. Scholl, P. Meyer, H.E. Killer, et al., The extracellular matrix composition of the optic nerve subarachnoid space, Exp. Eye Res. 200 (2020), https://doi.org/10.1016/J.EXER.2020.108250.
[40] L. Zhang, M.R. Beotra, M. Baskaran, T.A. Tun, X. Wang, S.A. Perera, et al., Vivo measurements of prelamina and lamina cribrosa biomechanical properties in humans, Invest. Ophthalmol. Vis. Sci. 61 (2020) 27, https://doi.org/10.1167/IOVS.61.3.27, 27.

[41] I. Issarti, C. Koppen, J.J. Rozema, Influence of the eye globe design on biomechanical analysis, Comput. Biol. Med. 135 (2021), https://doi.org/10.1016/j.compbiomed.2021.104612.
[42] P. Saboori, Subarachnoid space trabeculae architecture, Clin. Anat. 34 (2021) 40–50, https://doi.org/10.1002/CA.23635.
[43] H.E. Killer, H.R. Laeng, J. Flammer, P. Groscurth, Architecture of arachnoid trabeculae, pillars, and septa in the subarachnoid space of the human optic nerve: anatomy and clinical considerations, Br. J. Ophthalmol. 87 (2003) 777–781, https://doi.org/10.1136/BJO.87.6.777.
[44] P. Saboori, A. Sadegh, Material modeling of the head's subarachnoid space, Sci. Iran. 18 (2011) 1492–1499, https://doi.org/10.1016/j.scient.2011.11.032.
[45] Z.M. Suar, G. Fabris, M. Kurt, Isolation and immunofluorescent staining of fresh rat pia-arachnoid complex tissue for micromechanical characterization, Curr Protoc Neurosci 89 (2019) e83, https://doi.org/10.1002/CPNS.83.
[46] K. Chen, A.P. Rowley, J.D. Weiland, M.S. Humayun, Elastic properties of human posterior eye, J. Biomed. Mater. Res. 102 (2014) 2001, https://doi.org/10.1002/JBM.A.34858. –7.
[47] D.B. MacManus, B. Pierrat, J.G. Murphy, M.D. Gilchrist, Region and species dependent mechanical properties of adolescent and young adult brain tissue, Sci. Rep. 7 (2017) 1, https://doi.org/10.1038/s41598-017-13727-z, 2017;7:1–12.
[48] E. Pavlatos, Y. Ma, K. Clayson, X. Pan, J. Liu, Regional deformation of the optic nerve head and peripapillary sclera during IOP elevation, Invest. Ophthalmol. Vis. Sci. 59 (2018) 3779–3788, https://doi.org/10.1167/IOVS.18-24462.
[49] Y. Ma, E. Pavlatos, K. Clayson, X. Pan, S. Kwok, T. Sandwisch, et al., Mechanical deformation of human optic nerve head and peripapillary tissue in response to acute IOP elevation, Invest. Ophthalmol. Vis. Sci. 60 (2019) 913–920, https://doi.org/10.1167/IOVS.18-26071.
[50] A.S.C. Reis, N. O'Leary, M.J. Stanfield, L.M. Shuba, M.T. Nicolela, B.C. Chauhan, Laminar displacement and prelaminar tissue thickness change after glaucoma surgery imaged with optical coherence tomography, Invest. Ophthalmol. Vis. Sci. 53 (2012) 5819–5826, https://doi.org/10.1167/IOVS.12-9924.
[51] Y.S. Sim, J.W. Kwon, D. Jee, J.A. Choi, S.H. Ko, C.K. Park, Increased prelaminar tissue thickness in patients with open-angle glaucoma and type 2 diabetes, PLoS One 14 (2019), https://doi.org/10.1371/JOURNAL.PONE.0211641.
[52] Y.W. Kim, M.J.A. Girard, J.M. Mari, J.W. Jeoung, Anterior displacement of lamina cribrosa during valsalva maneuver in young healthy eyes, PLoS One 11 (2016), https://doi.org/10.1371/JOURNAL.PONE.0159663.
[53] S. Vurgese, S. Panda-Jonas, J.B. Jonas, Scleral thickness in human eyes, PLoS One 7 (2012), https://doi.org/10.1371/JOURNAL.PONE.0029692.
[54] F. Li, Q. Shang, G. Tang, H. Zhang, X. Yan, L. Ma, et al., Analysis of peripapillary and macular choroidal thickness in eyes with pseudoexfoliative glaucoma and fellow eyes, J Ophthalmol 2020 (2020), https://doi.org/10.1155/2020/9634543.
[55] W. Song, P. Huang, X. Dong, X. Li, C. Zhang, Choroidal thickness decreased in acute primary angle closure attacks with elevated intraocular pressure, Curr. Eye Res. 41 (2016) 526–531, https://doi.org/10.3109/02713683.2015.1037002.
[56] J.B. Jonas, L. Holbach, Central corneal thickness and thickness of the lamina cribrosa in human eyes, Invest. Ophthalmol. Vis. Sci. 46 (2005) 1275–1279, https://doi.org/10.1167/IOVS.04-0851.
[57] S.S. Hayreh, Anterior Ischemic Optic Neuropathy, Springer Berlin Heidelberg, Berlin, Heidelberg, 1975, https://doi.org/10.1007/978-3-642-65957-7.
[58] G. Wollensak, E. Spoerl, T. Seiler, Stress-strain measurements of human and porcine corneas after riboflavin-ultraviolet-A-induced cross-linking, J. Cataract Refract. Surg. 29 (2003) 1780, https://doi.org/10.1016/S0886-3350(03)00407-3. –5.
[59] M.H. Ross, Pawlina Wojciech, Histology : a Text and Atlas : with Correlated Cell and Molecular Biology, 2011, p. 974.
[60] E. Spoerl, A.G. Boehm, L.E. Pillunat, The influence of various substances on the biomechanical behavior of lamina cribrosa and peripapillary sclera, Invest. Ophthalmol. Vis. Sci. 46 (2005) 1286–1290, https://doi.org/10.1167/IOVS.04-0978.
[61] D.B. MacManus, J.G. Murphy, M.D. Gilchrist, Mechanical characterisation of brain tissue up to 35% strain at 1, 10, and 100/s using a custom-built micro-indentation apparatus, J. Mech. Behav. Biomed. Mater. 87 (2018) 256–266, https://doi.org/10.1016/J.JMBBM.2018.07.025.
[62] Z. Du, Z. Li, P. Wang, Z. Zhuang, Z. Liu, Revealing the nonlinear mechanical behavior of white matter brain tissue by analyzing the asynchronous deformation and damage of matrix and axonal fibers, Int. J. Solid Struct. (2022) 242, https://doi.org/10.1016/j.ijsolstr.2022.111554.
[63] P.C. Dechow, G.A. Nail, C.L. Schwartz-Dabney, R.B. Ashman, Elastic properties of human supraorbital and mandibular bone, Am. J. Phys. Anthropol. 90 (1993) 291–306, https://doi.org/10.1002/AJPA.1330900304.
[64] M.A. Zmuda Trzebiatowski, P. Kłosowski, A. Skorek, K. Żerdzicki, P. Lemski, M. Koberda, Nonlinear dynamic analysis of the pure "buckling" mechanism during blow-out trauma of the human orbit, Sci. Rep. 10 (2020), https://doi.org/10.1038/S41598-020-72186-1.
[65] K. Chen, J.D. Weiland, Mechanical properties of orbital fat and its encapsulating connective tissue, J. Biomech. Eng. 133 (2011), https://doi.org/10.1115/1.4004289.
[66] A. Karimi, R. Grytz, S.M. Rahmati, C.A. Girkin, J.C. Downs, Analysis of the effects of finite element type within a 3D biomechanical model of a human optic nerve head and posterior pole, Comput. Methods Progr. Biomed. (2021) 198, https://doi.org/10.1016/J.CMPB.2020.105794.
[67] M.A. Fazio, J.K. Johnstone, B. Smith, L. Wang, C.A. Girkin, Displacement of the lamina cribrosa in response to acute intraocular pressure elevation in normal individuals of african and European descent, Invest. Ophthalmol. Vis. Sci. 57 (2016) 3331–3339, https://doi.org/10.1167/IOVS.15-17940.
[68] P. Saboori, A. Sadegh, On the properties of brain sub arachnoid space and biomechanics of head impacts leading to traumatic brain injury, Advances in Biomechanics and Applications 1 (2014) 253–267, https://doi.org/10.12989/aba.2014.1.4.253.
[69] J.C. Downs, J.K.F. Suh, K.A. Thomas, A.J. Bellezza, C.F. Burgoyne, R.T. Hart, Viscoelastic characterization of peripapillary sclera: material properties by quadrant in rabbit and monkey eyes, J. Biomech. Eng. 125 (2003) 124–131, https://doi.org/10.1115/1.1536930.
[70] C.E.H. Scott, A.H.R.W. Simpson, P. Pankaj, Distinguishing fact from fiction in finite element analysis, Bone Joint Lett. J 102-B (2020) 1271, https://doi.org/10.1302/0301-620X.102B10.BJJ-2020-0827.R1. –3.
[71] E. Uchio, Y. Watanabe, K. Kadonosono, Y. Matsuoka, S. Goto, Simulation of airbag impact on eyes after photorefractive keratectomy by finite element analysis method, Graefes Arch. Clin. Exp. Ophthalmol. 241 (2003) 497–504, https://doi.org/10.1007/S00417-003-0679-8.
[72] L. Wang, G.A. Cull, C. Piper, C.F. Burgoyne, B. Fortune, Anterior and posterior optic nerve head blood flow in nonhuman primate experimental glaucoma model measured by laser speckle imaging technique and microsphere method, Invest. Ophthalmol. Vis. Sci. 53 (2012) 8303–8309, https://doi.org/10.1167/IOVS.12-10911.
[73] M.R. Beotra, X. Wang, T.A. Tun, L. Zhang, M. Baskaran, T. Aung, et al., In vivo three-dimensional lamina cribrosa strains in healthy, ocular hypertensive, and glaucoma eyes following acute intraocular pressure elevation, Invest. Ophthalmol. Vis. Sci. 59 (2018) 260–272, https://doi.org/10.1167/IOVS.17-21982.
[74] U.J. Ilg, Slow eye movements, Prog. Neurobiol. 53 (1997) 293–329, https://doi.org/10.1016/S0301-0082(97)00039-7.
[75] Types of eye movements and their functions - neuroscience - NCBI bookshelf n.d. https://www.ncbi.nlm.nih.gov/books/NBK10991/. (Accessed 19 July 2022) accessed.
[76] P. Saboori, A. Sadegh, Histology and morphology of the brain subarachnoid trabeculae, Anat Res Int 2015 (2015) 1–9, https://doi.org/10.1155/2015/279814.
[77] G. Cennamo, D. Montorio, M.A. Breve, V.B. Morra, F. Menna, G. Cennamo, Evaluation of optic nerve subarachnoid space in primary open angle glaucoma using ultrasound examination, PLoS One 13 (2018), https://doi.org/10.1371/JOURNAL.PONE.0208064.
[78] H. Liu, D. Yang, T. Ma, W. Shi, Q. Zhu, J. Kang, et al., Measurement and associations of the optic nerve subarachnoid space in normal tension and primary open-angle glaucoma, Am. J. Ophthalmol. 186 (2018) 128–137, https://doi.org/10.1016/J.AJO.2017.11.024.
[79] N. Wang, X. Xie, D. Yang, J. Xian, Y. Li, R. Ren, et al., Orbital cerebrospinal fluid space in glaucoma: the Beijing intracranial and intraocular pressure (iCOP) study, Ophthalmology 119 (2012), https://doi.org/10.1016/J.OPHTHA.2012.03.054.
[80] B.N. Nguyen, J.O. Cleary, R. Glarin, S.C. Kolbe, B.A. Moffat, R.J. Ordidge, et al., Ultra-high field magnetic resonance imaging of the retrobulbar optic nerve, subarachnoid space, and optic nerve sheath in emmetropic and myopic eyes, Transl Vis Sci Technol 10 (2021) 1–13, https://doi.org/10.1167/TVST.10.2.8.
[81] S. Schutte, S.P.W. van den Bedem, F. van Keulen, F.C.T. van der Helm, H.J. Simonsz, A finite-element analysis model of orbital biomechanics, Vis. Res. 46 (2006) 1724–1731, https://doi.org/10.1016/J.VISRES.2005.11.022.

[82] M.J.A. Girard, J.C. Downs, C.F. Burgoyne, J.K.F. Suh, Peripapillary and posterior scleral mechanics–part I: development of an anisotropic hyperelastic constitutive model, J. Biomech. Eng. 131 (2009), https://doi.org/10.1115/1.3113682.
[83] A.P. Voorhees, N.J. Jan, I.A. Sigal, Effects of collagen microstructure and material properties on the deformation of the neural tissues of the lamina cribrosa, Acta Biomater. 58 (2017) 278–290, https://doi.org/10.1016/J.ACTBIO.2017.05.042.
[84] N. Barshes, A. Demopoulos, H.H. Engelhard, Anatomy and physiology of the leptomeninges and CSF space, Cancer Treat Res. 125 (2005) 1–16, https://doi.org/10.1007/0-387-24199-X_1.